nature communications

Article

https://doi.org/10.1038/s41467-025-63048-3

Fatigue-free ferroelectricity in $Hf_{0.5}Zr_{0.5}O_2$ ultrathin films via interfacial design

Received: 17 March 2025

Accepted: 7 August 2025

Chao Zhou[1,8], **Yanpeng Feng**[2,8], **Liyang Ma**[3,8], **Haoliang Huang**[4], **Yangyang Si**[1], **Hailin Wang**[1], **Sizhe Huang**[1], **Jingxuan Li**[1], **Chang-Yang Kuo**[5], **Sujit Das**[6], **Yunlong Tang**[2,7] ✉, **Shi Liu**[3] ✉ & **Zuhuang Chen**[1] ✉

Due to traits of CMOS compatibility and scalability, HfO_2-based ferroelectric ultrathin films are promising candidates for next-generation low-power memory devices. However, their commercialization has been hindered by reliability issues, with fatigue failure being a major impediment. Here, we report superior ferroelectric performances with fatigue-free behavior in interface-designed $Hf_{0.5}Zr_{0.5}O_2$-based ultrathin heterostructures. A coherent $CeO_{2-x}/Hf_{0.5}Zr_{0.5}O_2$ heterointerface is constructed, wherein the oxygen-active, multivalent CeO_{2-x} acts as an “oxygen sponge”, capable of reversibly accepting and releasing oxygen ions. This design effectively alleviates defect aggregation at the electrode-ferroelectric interface and reduces coercive field, enabling improved switching characteristics and exceptional reliability. Further, a symmetric capacitor architecture is designed to minimize the imprint, thereby suppressing the oriented oxygen defect drift. The two-pronged technique prevents intense fluctuations of oxygen concentration within the device during electrical cycling, suppressing the formation of paraelectric phase and polarization degradation. The interfacial design technique ensures superior switching and cycling performances of $Hf_{0.5}Zr_{0.5}O_2$ capacitors, embodying a fatigue-free feature exceeding 10^{11} switching cycles and an endurance lifetime surpassing 10^{12} cycles, along with excellent temperature stability and long retention. These findings pave the way for the development of high-performance and ultra-stable hafnia-based ferroelectric devices.

Ferroelectric memories elicit great interests for the merits of reversible polarization states[1], nonvolatile characteristic[1], fast switching speed[2], and low energy consumption[3–5], all of which cater to the demands of next-generation low-power memory and logic devices, such as ferroelectric random access memory[3,6], ferroelectric field-effect transistors[7–9], as well as emerging computing paradigms like neuromorphic and in-memory computing[10]. The exceptional ferroelectricity discovered in the high-κ dielectric HfO_2-based ultrathin films[11], which are fully compatible with Si-technologies and overcome the thickness limitation[12,13], provides a solution to tackle the CMOS compatibility and

---

[1] State Key Laboratory of Precision Welding and Joining of Materials and Structures, School of Materials Science and Engineering, Harbin Institute of Technology, Shenzhen, China. [2] Shenyang National Laboratory for Materials Science, Institute of Metal Research, Chinese Academy of Sciences, Shenyang, China. [3] Department of Physics, School of Science, Westlake University, Hangzhou, Zhejiang, China. [4] Quantum Science Center of Guangdong-Hong Kong-Macao Greater Bay Area, Shenzhen, China. [5] Department of Electrophysics, National Yang Ming Chiao Tung University, Hsinchu, Taiwan. [6] Materials Research Centre, Indian Institute of Science, Bangalore, India. [7] School of Materials Science and Engineering, University of Science and Technology of China, Shenyang, China. [8] These authors contributed equally: Chao Zhou, Yanpeng Feng, Liyang Ma. ✉e-mail: yltang@imr.ac.cn; liushi@westlake.edu.cn; zuhuang@hit.edu.cn

scalability concerns inherent in conventional perovskite oxide ferroelectrics[14,15]. Since its discovery, HfO_2-based ferroelectrics have greatly facilitated the integration of ferroelectricity into integrated circuits and boosted the progress of ferroelectric memories[16]. Despite that, reliability characteristics of HfO_2-based ferroelectric electronics, particularly fatigue resistance[6,17], fall short of commercial metrics[18]. It is well established that a stable polarization state is fundamental to the operation of ferroelectric devices. Nevertheless, fatigue, characterized by a decrease in switchable polarization during repeated read-write operations, renders polarization states indiscernible and ultimately leads to device malfunction. Till now, most HfO_2-based planar capacitor devices can only sustain a stable cycling behavior for ~10^6 cycles[19–22]. This is considerably lower than those of perovskite oxide counterparts (such as $SrBi_2Ta_2O_9$[23], $Bi_{3.25}La_{0.75}Ti_3O_{12}$[24], and $PbZr_xTi_{1-x}O_3$[25,26]), which can bear steady performances for >10^{10} switching cycles[25,27]. Additionally, other reliability-related concerns, such as endurance, retention and temperature stability, continue to pose obstacles[4]. Altogether, these reliability issues present substantial impediments to advancing high-performance HfO_2-based ferroelectric devices.

Several models have been proposed to explain the fatigue degradation mechanism[19,28,29]. Field-driven defect generation and migration, particularly of oxygen vacancies (V_O), along with consequent defect trapping and accumulation, are often attributed to these performance instabilities. Especially, several unique features inherent in the unconventional polar phase of HfO_2 likely cause its increased susceptibility to fatigue. The ferroelectric phase of HfO_2 (orthorhombic $Pca2_1$), compared to the ground-state monoclinic $P2_1/c$ paraelectric phase, is metastable[30], and would transition into the nonpolar phase when subjected to disturbances like oxygen voltammetry[31] during electrical cycling. Additionally, the high coercivity characteristic of HfO_2-based ferroelectrics[13] provides sufficient driving force for the generation and migration of V_O[32], which accelerates fatigue. The ultra-thin thickness of HfO_2-based ferroelectric film not only amplifies these effects, but also makes the interfacial-related degradations (like domain pinning and phase transition) more

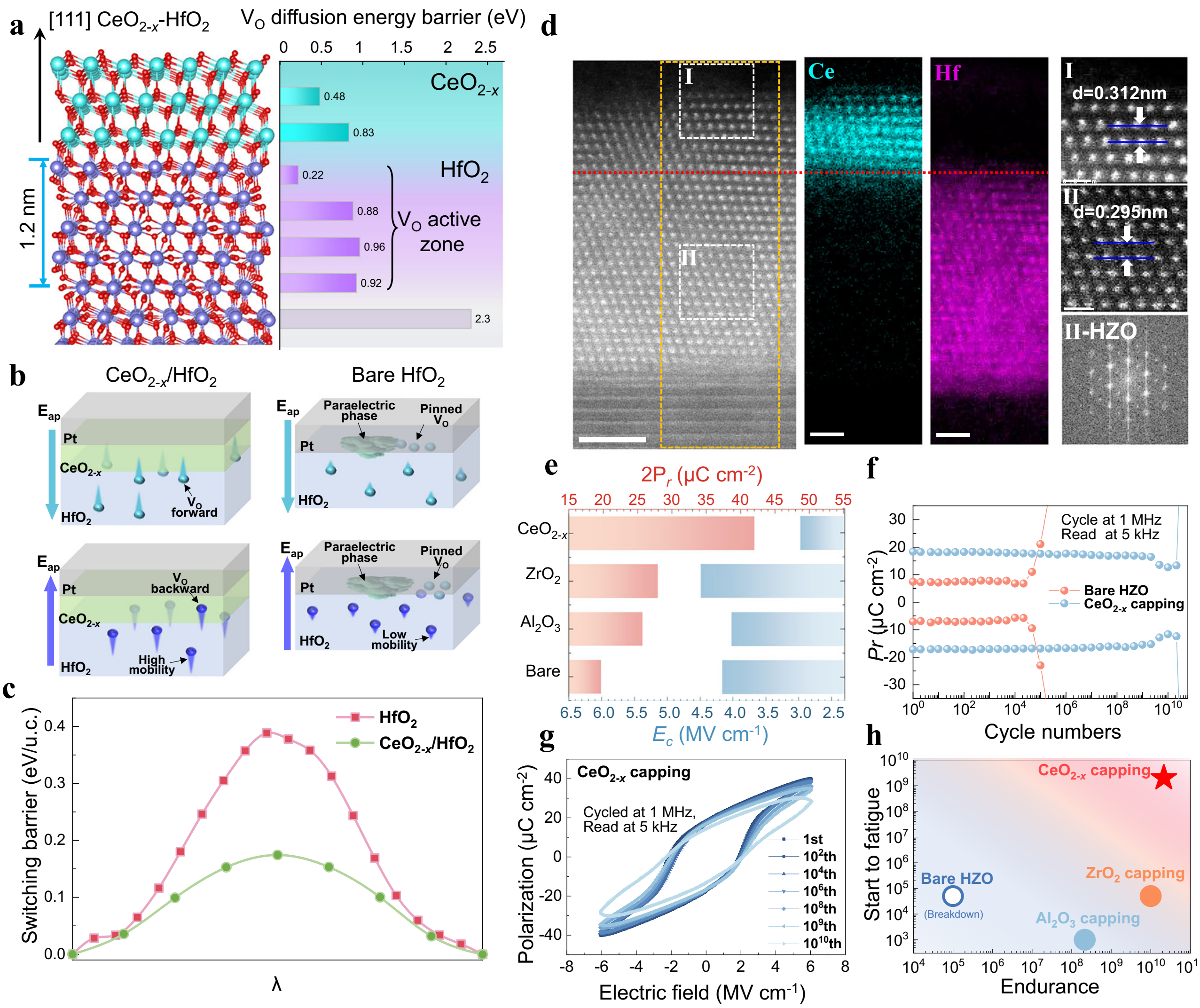

Fig. 1 | Atomic insight and enhanced performances of interface-designed HfO_2-based devices. a Diffusion energy barriers of oxygen vacancy (V_O) in the CeO_{2-x}/HfO_2 heterostructure. **b** Schematics of V_O migrations in the capacitors based on CeO_{2-x}/HfO_2 and bare HfO_2 under fields. The arrows colored in cyan and blue denote the applied electric fields in different directions. The spheres highlighted in cyan and blue represent the oxygen vacancies moving forward and backward. The length of the tails, irrespective of color, signifies the mobility of defects in the presence of external electric fields. **c** Polarization switching barriers for the CeO_{2-x}/HfO_2 and bare HfO_2 capacitors. **d** HADDF-STEM image, EELS mappings and Fourier transformation for the CeO_{2-x}/HfO_2/LSMO heterostructures. **e** Coercive fields and remnant polarization values for capped HZO devices. **f** Cycling performances for the bare Pt/HZO/LSMO device and Pt/CeO_{2-x}/HZO/LSMO capacitor. **g** Polarization-electric field loops for the Pt/CeO_{2-x}/HZO/LSMO capacitor at different cycling stages. **h** A comparison of the fatigue and endurance behaviors for the HZO-based capacitors with different capping layers.

pronounced. These aspects collectively trigger an early fatigue during operations. Strategies like oxygen scavenging[33,34], oxygen supply[35,36], and electrical rejuvenation[37], aimed at maintaining the metastable polar phase, reducing defect segregation and releasing pinned domains during cycling, have shown some success in enhancing endurance and relieving fatigue. However, cycling behaviors of optimized HfO_2-based planar capacitor devices still lag far behind those of commercial perovskite oxide-based ferroelectric devices[4,32]. A deeper understanding of the underlying mechanisms of fatigue and further optimization of the reliability of HfO_2-based ferroelectrics are urgently needed.

Here, we demonstrate a well-designed interface that can drastically improve the reliability characteristics of HfO_2-based ultrathin ferroelectric devices. An ultrathin fluorite-structured CeO_{2-x} is engineered as a coherent capping layer on ferroelectric $Hf_{0.5}Zr_{0.5}O_2$ (HZO) film, effectively reducing the switching barrier during polarization reversals. Moreover, the multivalent-oxide CeO_{2-x} epitaxial layer not only reduces the diffusion barrier of V_O near the CeO_{2-x}/HZO interface region but also serves as an "oxygen-sponge", which can reversibly accept and release V_O. This approach mitigates the ferroelectric-to-paraelectric phase transformation and maintains the polar feature of HZO throughout the cycling process, yielding an ultra-thin CeO_{2-x}/HZO heterojunction ferroelectric device with notably enhanced polarization ($P_r = 21\,\mu C\,cm^{-2}$) and reduced coercive field (<3 $MV\,cm^{-1}$ for the 6 nm film), alleviated imprint and stable retention. Furthermore, incorporating an additional $La_{0.67}Sr_{0.33}MnO_3$ (LSMO) layer on the CeO_{2-x} film as a secondary buffer constructs a more symmetric capacitor (i.e., Pt/LSMO/CeO_{2-x}/HZO/LSMO). This design suppresses the imprint field-driven oriented defect movement, enables comprehensive improvement of ferroelectric properties and achieves an ultra-stable cycling behavior of hafnia-based devices, which manifests as a fatigue-free cycling behavior approaching 10^{11} electrical cycles and a stable endurance lifetime surpassing 10^{12} cycles.

Results

DFT computational results

It is well known that ferroelectric-electrode heterointerfaces, where defect accumulation[28], charge injection[38], and domain pinning[39,40] occur, are crucial to the cycling reliability of ferroelectric materials. These interfacial phenomena would play an important role in the endurance and fatigue behaviors of HfO_2-based ferroelectric devices. Therefore, optimizing interfaces is a natural and feasible strategy for enhancing reliability.

We choose fluorite-structured CeO_{2-x} as the optimal interfacial buffer for HfO_2 because of its structural similarity to HfO_2 and its oxygen-active properties[41–43]. Our first-principles calculations reveal that the migration barrier for V_O in bulk HfO_2 is ~2.3 eV (Fig. 1a). Notably, the incorporation of a CeO_{2-x}/HfO_2 interface activates V_O in HfO_2 near the interface region (~1.2 nm thick based on our DFT calculations), substantially reducing the V_O diffusion barrier to a range of 0.22–0.96 eV. Therefore, V_O becomes mobile in the interface zone, alleviating the defect pinning and enabling an effortless movement of V_O across the CeO_{2-x}/HfO_2 heterointerface. The CeO_{2-x} buffer, by promoting interfacial vacancy mobility, effectively serves as an "oxygen sponge", rendering the reversible storage and release of V_O during electrical read-write operations. As schematized in Fig. 1b, this oxygen-active CeO_{2-x}/HfO_2 heterointerface facilitates the timely transportation of V_O under electric fields. In this configuration, the CeO_{2-x} layer, rather than the HfO_2 film, acts as the source and drain of V_O, preventing the accumulated change of oxygen concentration within HfO_2. This design could maintain the metastable polar HfO_2 phase and mitigate the early degradation of switching performance of HfO_2-based ferroelectric devices. Conversely, other interfaces, such as ZrO_2/HfO_2 (Supplementary Fig. S1) or bare HfO_2 (Fig. 1b), are less competent in activating V_O. This inefficiency leads to the aggregation of defects near the interface, likely causing domain pinning and phase transition during cycling operations. Furthermore, our DFT calculations suggest that the higher symmetry of the cubic CeO_{2-x} layer lowers the energy of the transition tetragonal state during polarization reversal, thereby reducing the switching barrier that scales with the energy difference between the orthorhombic ferroelectric phase and the tetragonal transition state. Consequently, the switching barrier for the CeO_{2-x}/HfO_2 heterostructure is decreased significantly (Fig. 1c), contributing to a smaller coercive field and enhanced endurance performance.

Characterizations of capped $Hf_{0.5}Zr_{0.5}O_2$

In accordance with the computational guidance, a ~ 6-nm-thick HZO film capped with ~0.8 nm CeO_{2-x} layer was fabricated (detailed in the "Methods" part). Additionally, HZO films with a capping layer of either ZrO_2 or Al_2O_3 oxides were also prepared for comparisons (Supplementary Fig. S2). XRD $\theta - 2\theta$ scans reveal that all films, grown on (001)-oriented LSMO/$SrTiO_3$, exhibit the (111) orientation of the orthorhombic ferroelectric phase with essentially identical diffraction peak positions (Supplementary Fig. S2b). Additionally, clear Laue oscillations near the $(111)_O$ diffraction peak of HZO and smooth film surfaces (Supplementary Fig. S2c–f) indicate high crystalline quality and a clean interface of the heterostructures. High-angle annular dark-field (HAADF) scanning transmission electron microscopy (STEM) and electron energy loss spectroscopy (EELS) mappings were further performed to characterize the structure and interface abruptness. An atomic-resolved image of the CeO_{2-x}/HZO heterostructure is presented (Fig. 1d), where a thicker CeO_{2-x} capping layer (~1.5 nm) was grown on the HZO to ensure clear observation. HAADF-STEM image demonstrates that the CeO_{2-x}/HZO heterointerface is coherent. Further analysis using EELS elemental mapping reveals a distinct interface and minimal interdiffusion within the CeO_{2-x}/HZO heterointerface.

Though structurally similar, the electrical performances of these heterostructures vary significantly. Compared to bare HZO films, capacitors based on HZO films with ZrO_2, Al_2O_3, and CeO_{2-x} capping layers exhibit notably lower leakage currents (Supplementary Fig. S3a). The differences in polarization switching characteristics are even more pronounced. The positive-up-negative-down (PUND) measurement reveals that all capped HZO devices show enhanced polarizations compared to the bare one (Supplementary Fig. S3b, c and Fig. 1e). Among them, capacitors based on CeO_{2-x}/HZO heterostructures demonstrate the most impressive performance, characterized by the highest remnant polarization ($P_r = 21\,\mu C\ cm^{-2}$), the sharpest polarization switching current and the lowest coercive field ($E_C = 2.9\,MV\,cm^{-1}$). Conversely, the effects of lowering E_C and enhancing P_r in HZO-based devices capped with either Al_2O_3 or ZrO_2 are less pronounced. These results are consistent with our aforementioned computational predictions. Furthermore, the CeO_{2-x}/HZO heterostructure exhibits the highest dielectric constant and most distinct butterfly-shaped ε-E curve (Supplementary Fig. S3e).

Benefiting from reduced leakage response, the breakdown strength and endurance capabilities of these capped capacitors have been substantially enhanced (Supplementary Fig. S4), in stark contrast to the early breakdown occurring after ~10^5 switching cycles in the bare HZO capacitors. However, the fatigue behaviors of ZrO_2/HZO and Al_2O_3/HZO devices still exhibit an average performance in comparison to reported results[19,20,22]. A noticeable degradation occurs in the early stage of cycling for both ZrO_2/HZO and Al_2O_3/HZO heterostructures, with a drastic decrease in polarization observed after 10^8 cycles (Supplementary Fig. S4e). Switching dynamics characterizations (Supplementary Fig. S5) are well consistent with the fatigue measurements of these HZO-based capacitors, manifested as the loss of polarization and the slowdown of switching speed after cycling. This may be attributed to the defect pinning and phase transitions occurring during the electrical cycling. In contrast, the "oxygen sponge" CeO_{2-x} buffer reduces V_O diffusion barrier and decreases coercive field

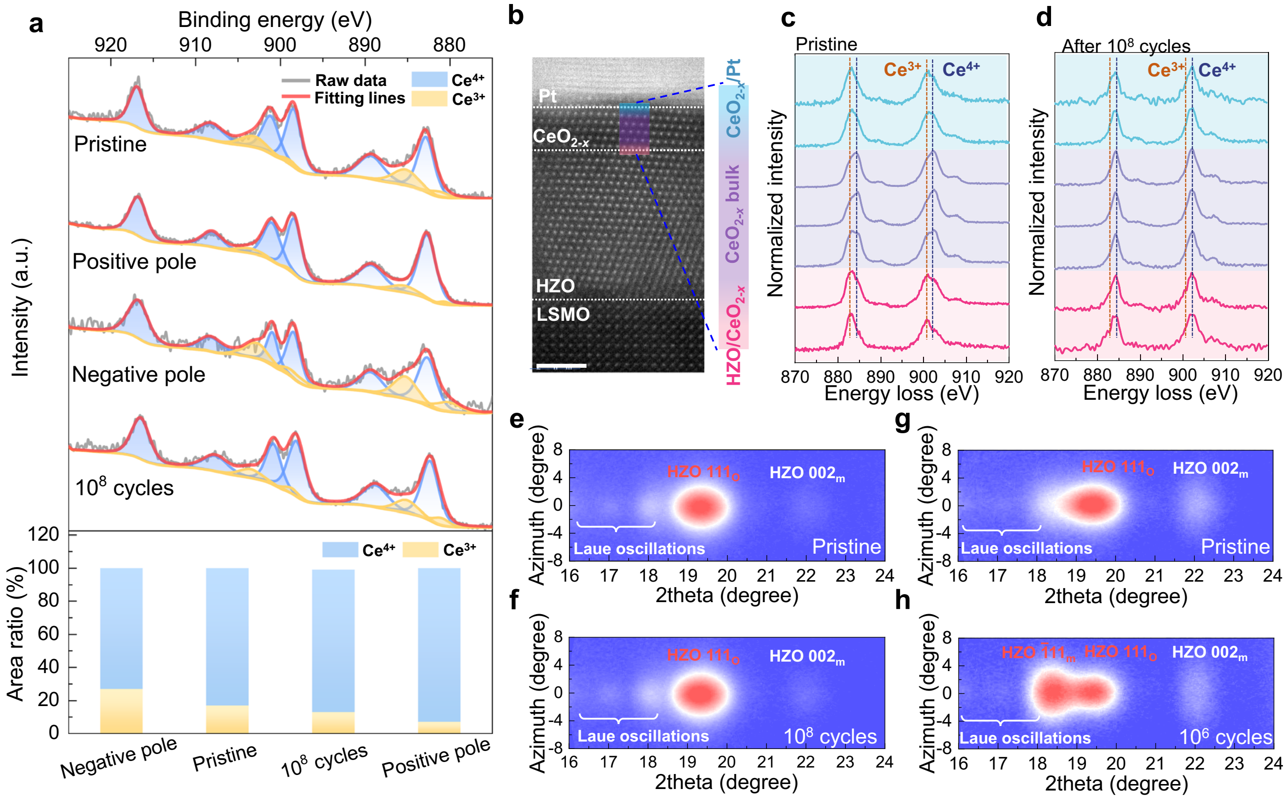

Fig. 2 | Evolution of Ce valence states and structure under different electric treatments. a Micro-area X-ray photoelectron spectroscopy (XPS) of the Ce element in the CeO_{2-x}/HZO heterostructure after different electric treatments and a summary of Ce^{3+}:Ce^{4+} ratio for the corresponding treatments. **b**–**d** HAADF-STEM image with the marked region for electron energy loss spectroscopy (EELS) measurements, along with the relevant EELS signals before and after endurance cycles. Micro-beam diffraction results for **e**, **f** the CeO_{2-x}/HZO film and **g**, **h** the bare HZO film before and after endurance cycles. The micro-beam diffractions were performed at the BL15U1 station in Shanghai Synchrotron Radiation Facility with a wavelength of 1 Å.

in the CeO_{2-x}/HZO device, which jointly ensure the exceptional reliability: the CeO_{2-x}/HZO-based capacitor demonstrates robust cycling stability, maintaining stable performance for over 2×10^9 cycles and an endurance lifespan exceeding 2×10^{10} cycles (Fig. 1f–h) as well as a stable dynamics profile (Supplementary Fig. S5e). This positions it among the most reliable categories of documented metal–ferroelectric–metal (MFM) planar devices[19,20,22].

Oriented drift of defects

To elucidate the impact of the CeO_{2-x} capping layer, semi in-situ micro-area X-ray photoelectron spectroscopy was employed to probe the valence state of CeO_{2-x}/HZO before and after electrical poling (Fig. 2a and Supplementary Fig. S6). For the as-grown state, the Ce cation within the CeO_{2-x} capping layer exhibits a multivalent oxidation state comprising both Ce^{3+} and Ce^{4+}, with the Ce^{3+} peak area constituting a modest ~17% of the total area. Remarkably, the trivalent (Ce^{3+}) and tetravalent (Ce^{4+}) oxidation states can interconvert under different electrical stimuli. Specifically, the area ratio of Ce^{3+} decreases to ~7% after positive poling, which indicates that a certain amount of V_O migrates from the CeO_{2-x} buffer toward the bottom LSMO electrode. Conversely, a significant amount of Ce^{4+} transitions into Ce^{3+} within the CeO_{2-x} layer under a negative bias. This phenomenon is corroborated by the Hf 4*f* XPS spectrum (Supplementary Fig. S7). Thanks to the protection of a CeO_{2-x} buffer layer, the Hf 4*f* spectrum exhibits less sensitivity to external bias compared to that of the bare HZO sample. In the case of the bare HZO counterpart, the sub-oxide peak emerging after negative pulse treatment (Supplementary Fig. S8) exhibits a markedly enhanced intensity compared to that observed in the CeO_{2-x}/HZO heterostructure. Collectively, these findings elucidate the "oxygen sponge" characteristic of the CeO_{2-x} layer during electrical operations, highlighting its ability to dynamically regulate V_O concentration within HZO, and thereby enhancing device performance and reliability.

Both computational and experimental results corroborate the reservoir feature of the CeO_{2-x} capping layer, which facilitates the reversible diffusion of V_O in accordance with the orientation of the applied electric field. Ideally, the reversible migration of the V_O would maintain a relatively stable oxygen content within the CeO_{2-x}/HZO device, thereby ensuring that the state of the ferroelectric capacitor would not vary significantly during cycling. This is a pivotal factor in sustaining the cycling reliability. Nevertheless, the peak area associated with Ce^{3+} decreases from ~17 to ~13% when the device undergoes 10^8 switching cycles (Fig. 2a). This signifies a net migration of V_O towards the LSMO bottom electrode and an accumulation of oxygen ions in the CeO_{2-x} capping layer, despite the capacitor being subjected to the symmetric bipolar electric field cycling. This phenomenon is further corroborated by the Ce $M_{4,5}$-edge EELS spectra. Initially, Ce^{3+} ions reside at the CeO_{2-x}/HZO heterointerface and extend into the bulk region of the CeO_{2-x} layer (Fig. 2c). After 10^8 cycles, the Ce^{3+} region becomes narrowed and the signature of Ce^{4+} intensifies (Fig. 2d), supporting the XPS results. The progressively oxygen-rich CeO_{2-x} layer would eventually lose its "oxygen sponge" function, ultimately leading to an inevitable fatigue of the CeO_{2-x}/HZO device after 2×10^9 cycles.

Synchrotron-based micro-beam XRD studies were further carried out to probe the possible phase transition during the fatigue process. The CeO_{2-x} buffer, functioning as a source and drain for V_O and oxygen ions, prevents the accumulation of V_O or oxygen atoms at the interface. Thus, the HZO layer in the heterostructure retains a stable polar

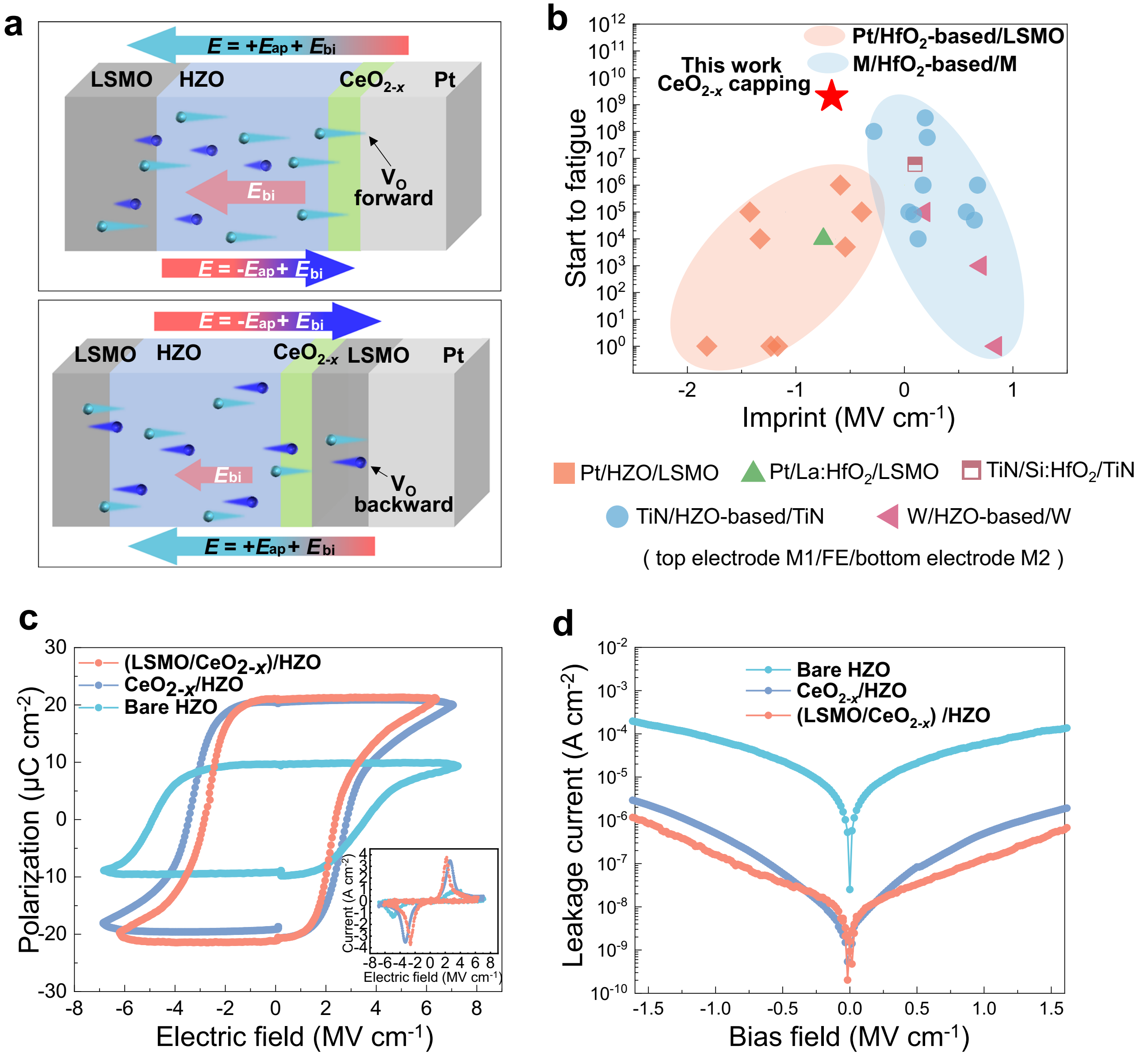

Fig. 3 | Effects of the HZO capacitor architecture on the electric performances. **a** Schematics depicting the impact of capacitor structure on the built-in bias (E_{bi}) and its influence on the external electric fields applied in different orientations. The pink arrows within the schematic diagrams of the films denote the E_{bi}, with their sizes indicating the magnitude of E_{bi}. The multicolored arrows external to the films represent the composite electric field, formed by the superposition of E_{bi} and the applied electric field (E_{ap}), with the length of the arrow proportionally representing the magnitude of the composite field. Spheres of varying colors are indicative of V_O undergoing forward and reverse migration, respectively, with the length of the tails signifying the degree of mobility. **b** Illustration of fatigue behaviors for capacitors with various architectures and imprints. **c**, **d** Positive-up negative-down (PUND) curves and leakage current measurements for HZO devices with diverse structural designs.

structure even after 10^8 cycles (Fig. 2e, f). In contrast, for Pt/HZO/LSMO capacitors without the CeO_{2-x} capping layers, due to the absence of a timely transportation of defects, the Pt/HZO interface acts as a terminal for defects and mobile ions, turning the HZO film itself becoming the main "battlefield". This leads to a gradual transformation of the metastable polar structure into the energetically favored phase due to the field cycling-induced chemical/energy fluctuations. Oxygen accumulation would occur at the Pt (top electrode)/HZO interface and induce the formation of the energetically stable paraelectric monoclinic phase when the bare HZO device cycled 10^6 times (to breakdown) (Fig. 2g, h). This observation is consistent with a previous study[31,44]. Therefore, the absence of oxygen-active CeO_{2-x} buffer layer leads to structural phase transitions and likely defect pinning at the interface, directly contributing to the fatigue phenomenon.

Behaviors of more symmetric capacitors

The oriented net movement of V_O or oxygen ions is usually attributed to the asymmetric electrical potential within the ferroelectric capacitor, leading to the asymmetric polarization and defect accumulation at the interface[45]. Tracing back to the PUND hysteresis loop of the Pt/CeO_{2-x}/HZO/LSMO capacitor (Supplementary Fig. S3), we can observe an apparent imprint (i.e., horizontal shift of the *P*–*E* loop) towards the negative bias, indicating the presence of a positive built-in field (E_{bi}), directed from the top electrode towards the bottom. This fixed positive E_{bi} superimposes on the applied external symmetric bipolar field ($\pm E_{ap}$), resulting in an asymmetric electrical potential, manifested as $(+E_{ap} + E_{bi})d$ and $(-E_{ap} + E_{bi})d$ (where *d* denotes the thickness of the ferroelectric), across the two-terminated capacitor per cycle (schematic illustrated in Fig. 3a). In this scenario, V_O or oxygen ions move back and forth but with

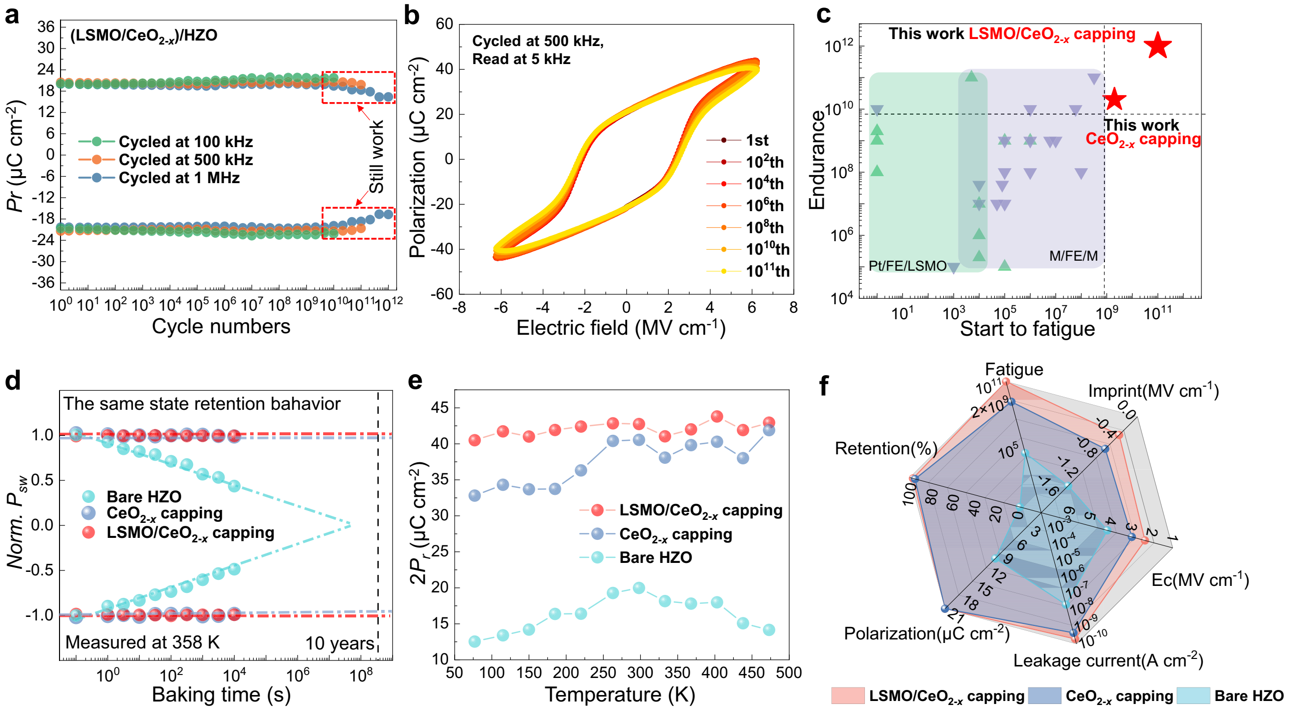

Fig. 4 | Reliability performances for the Pt/LSMO/CeO$_{2-x}$/HZO/LSMO capacitor. **a** Endurance and fatigue behaviors for the LSMO/CeO$_{2-x}$/HZO/LSMO device at different cycling frequencies. **b** Polarization–electric field loops of the capacitor at different cycling stages. **c** Comparison of the endurance and fatigue manners for different HZO-based planar capacitors. **d**–**f** Retention results (recording the normalized switchable polarizations (*Norm.P*$_{sw}$) as a function of baking time), temperature stability and overall comparisons of electric performances for HZO capacitors with different interfacial designs.

different velocities and distances under the electrical driving force with different polarities, triggering the directional migration of V_O or oxygen ions. Herein, Fig. 3b summaries the relationship between the imprint and fatigue behaviors in representative studies (Supplementary Note 1 for references). Interestingly, an empirical trend emerges: the more severe the imprint, the faster the onset of fatigue. This correlation aligns with our prior elucidations that the noticeable imprint provides sufficient driving force for the directional movement of defects.

Figure 3b further demonstrates that the architecture of a ferroelectric capacitor influences the imprint effect. A symmetric capacitor structure can effectively decrease the imprint effect. Therefore, it is logical to consider the symmetric "Pt/LSMO/HZO/LSMO" capacitor architecture (Supplementary Fig. S9), where the HZO layer is sandwiched between two LSMO films, for improved reliability. Owing to the symmetric capacitor structure, the LSMO-capped HZO specimen does exhibit reduced E_C and a smaller imprint (Supplementary Fig. S10). These factors contribute to the enhanced cycling performance of the LSMO/HZO/LSMO device, outperforming ZrO_2 and Al_2O_3-capped counterparts. Despite that, the fatigue behavior of the Pt/LSMO/HZO/LSMO capacitor is still inferior to that of the Pt/CeO$_{2-x}$/HZO/LSMO counterpart (Supplementary Fig. S10d). We propose that this is probably due to the lower effectiveness of V_O transport in LSMO compared to CeO$_{2-x}$[46,47].

To fully leverage the benefits of the symmetric structure while simultaneously maintaining a reduced V_O interfacial diffusion barrier, we further grow the LSMO layer on top of the CeO$_{2-x}$ (Supplementary Fig. S11). The LSMO layer not only serves as a secondary oxygen reservoir but also plays a vital role in minimizing the imprint effect. As expected, the ultrathin Pt/LSMO/CeO$_{2-x}$/HZO/LSMO capacitor exhibits a low E_C of 2.34 MV cm^{-1} and suppressed imprint effect (with E_{bi} of only 0.38 MV cm^{-1}) (Fig. 3c and Supplementary Fig. S12). Accordingly, the oriented drift of defects in the Pt/LSMO/CeO$_{2-x}$/HZO/LSMO capacitor is suppressed compared to that of the Pt/CeO$_{2-x}$/HZO/LSMO capacitor (Supplementary Fig. S13). Additionally, the insertion of the LSMO layer on the CeO$_{2-x}$ buffer does not exacerbate the leakage current (Fig. 3d).

The synergistic effects of the reduced V_O migration barrier, the LSMO-CeO$_{2-x}$ bilayer "oxygen sponge" and the mild imprint collectively enable remarkable cycling performance of the Pt/LSMO/CeO$_{2-x}$/HZO/LSMO ferroelectric capacitor, demonstrating virtually fatigue-free behavior for up to 10^{11} cycles (the capacitor shows little change in the hysteresis loop and there is only a < 5% loss in polarization after the 10^{11} switching cycle) and maintaining a stable ferroelectricity even after 10^{12} cycles (Fig. 4a, b and Supplementary Fig. S14a,b). Meanwhile, pulse switching dynamics measurement (Supplementary Fig. S14c) demonstrates a tiny variation of switchable polarization and switching time after field cycling. To our knowledge, this interface-designed device exhibits the most robust stability without requiring any rejuvenation process[37,48] during fatigue measurements, making it the most stable HfO_2-based planar capacitor reported to date (Fig. 4c and Supplementary Note 1 for references). Beyond that, the fine interface condition, robust phase stability, and mitigated imprint achieved through the interfacial design strategy not only reinforce the resistance against thermal depolarization, but also sustain the memory margin that might otherwise be narrowed by the imprint shift[49]. Therefore, the Pt/LSMO/CeO$_{2-x}$/HZO/LSMO capacitors display stable retention capabilities, encompassing the same state (SS) and opposite state (OS)[50] retention behaviors (Fig. 4d and Supplementary Fig. S15), with accelerated aging tests at 358 K projecting stable performance beyond the 10-year benchmark. What's more, distinct from the intense changes in polarization observed in other HZO-based ferroelectric devices[51,52] in varying temperatures, our device exhibits reliable temperature stability (Fig. 4e and Supplementary Fig. S16).

Discussion

The reliability issue, especially the fatigue failure, is one of the key limitations that need to be settled for hafnia-based ferroelectric devices. Here, the oxygen-active and "oxygen sponge" characteristics brought by the CeO_{2-x}/HZO heterointerface effectively suppress the defect accumulation and consequent polar-paraelectric phase transition during the field cycling. These enable ferroelectric devices based on the CeO_{2-x}/HZO heterostructure with enhanced polarization, impressive fatigue-resistance and endurance behaviors. Our systematic studies further reveal the detrimental impact of directional defect migration caused by the built-in field (imprint) on fatigue characteristics. By further building a more symmetric-structure capacitor, a record-breaking fatigue-free HfO_2-based planar capacitor, which can be steadily operated over 10^{12} cycles, is obtained. In addition, the designed device demonstrates a comprehensive improvement of ferroelectric properties which can be defined as the "hexagonal warrior" in view of its attractive traits of fatigue-resistant, retention, coercive field, leakage current, imprint and switchable polarization (Fig. 4f) and the comprehensive reliability performances of this simple designed planar capacitor are even exceeding those of Micron's very recent device with advanced 3D integration and complicated packaging solutions[16]. Through the design of a symmetric-structure capacitor with an "oxygen sponge" layer, we have harnessed the migration of V_O/oxygen ions during the cycling operation, achieving ideal performances of HfO_2-based ferroelectric devices. It should be noted, however, that our current fabrication process requires large thermal budgets during sample preparation, and the use of complex LSMO perovskite oxide presents compatibility challenges with Si-based technologies. Despite these limitations, our work elucidates the fatigue mechanism and develops a well-interfacial design strategy that drastically improves the reliability characteristics of HZO epitaxial thin films. Not only does this work deepen our understanding of hafnia ferroelectrics, but it also lays a firm foundation for utilizing this emergent CMOS-compatible ferroelectric for widespread applications, such as nonvolatile memory devices.

Methods

Sample deposition

Both the LSMO (22 nm)/CeO_2 (0.8 nm)/HZO (6 nm)/LSMO (11 nm) and CeO_2 (0.8 nm)/HZO (6 nm)/LSMO (11 nm) systems were epitaxially grown on (001) $SrTiO_3$ single crystal substrates by pulsed laser deposition (Arrayed Materials RP-B) using a KrF excimer laser (λ = 248 nm). The HZO layers were deposited at 600 °C under an oxygen partial pressure of 15 Pa at a laser repetition rate of 2 Hz and a laser fluence of 1.35 J cm^{-2}. The CeO_{2-x} were fabricated at an oxygen pressure of 10 Pa at 600 °C with a laser fluence of 0.85 J cm^{-2} and a laser repetition rate of 3 Hz. The bottom electrode LSMO layers were grown with a laser (3 Hz, 0.85 J cm^{-2}) under an oxygen partial pressure of 20 Pa at the substrate temperature of 700 °C. For the top LSMO capping layers, they were deposited at 600 °C with a laser (3 Hz, 0.85 J cm^{-2}) under an oxygen partial pressure of 20 Pa.

Device fabrication

All films were processed with a standard lithography to pattern the top electrode mask on the films. After photolithography, the top electrode Pt layer was deposited on the mask areas via magnetron sputtering (Arrayed Materials RS-M). The MFM structure capacitors were fabricated when the photoresist was lifted off. As for LSMO-capped devices, the LSMO exposed area that was not covered by Pt was etched by the KI + HCl solution (0.37% HCl + 5 mol L^{-1} KI aqueous solution).

Micro-area XPS characterizations

The micro-area X-ray photoelectron spectroscopy was performed using a PHI VersaProbe four instrument (Physical Electronics, Inc.) on capacitors with a diameter of 50 µm. In the XPS analysis, energy calibration was carried out by using the C 1*s* peak at 284.8 eV.

X-ray diffraction and topography characterizations

X-ray θ–2θ scans were obtained by a high-resolution X-ray diffractometer (Rigaku Smartlab 9 kW). To study the phase structure of HZO heterostructures before and after electric treatments, micro-area XRD was carried out at the beamline BL15U1 station in Shanghai Synchrotron Radiation Facility (SSRF) on capacitor devices with a diameter of 25 µm. The wavelength and diameter of the X-ray are 1 Å and 5 µm. The obtained data was explored and processed with the *Dioptas* programs suit[53]. The film morphology was determined by an Asylum Research MFP-3D-Infinity atomic force microscope.

Aberration-corrected STEM characterization

The TEM samples for STEM observations were prepared by the focused-ion-beam lift-out method. Before cutting, the C and W coatings were deposited on the devices to protect the surface of the devices. At first, the voltage of 30 kV and current of 0.44 nA for the ion beam were used to polish the TEM samples. Then the current was gradually reduced to 41 pA. Finally, the voltages of 5 kV, 2 kV, and 1 kV for the ion beam were used to clean the surface amorphously. Cross-sectional HAADF-STEM images and EELS mappings were acquired by a double-aberration-corrected scanning transmission electron microscope (Spectra 300, ThermoFisher Scientific) equipped with a monochromator, a Gatan 1069 EELS system and a K3 camera operating at 300 kV.

Electrical characterizations

Electrical measurements were implemented via an MFM capacitance structure with the bottom electrode LSMO grounded and the top electrode Pt (with a diameter of 25 µm) connected to the driving end. The electric performances, including dynamic P–E loops, PUND measurements, retention measurements and fatigue behaviors, were measured using a TF 3000 analyzer (aixACCT) and leakage currents were measured using a Keithley 4200A-SCS parameter analyzer (Tektronix). All temperature-dependent measurements were carried out in a cryogenic probe station (TTPX, Lake Shore Cryotronics).

DFT calculations

All first-principles density functional theory calculations were performed using Vienna Ab initio Simulation Package (VASP) with generalized gradient approximation of the Perdew–Burke–ErnZerhof type[54–56]. To describe the localized 4*f* states of Ce properly, the on-site Coulomb interaction correction was used[57]. As suggested by previous works, the U value for Ce 4*f* was set to 5.0 eV[58,59]. The optimized lattice constants of CeO_2 are $a = b = c = 5.50$ Å for the cubic phase, in good agreement with the experimental value (5.411 Å). In order to better fit the experimental conditions, we construct a (111)-orientation interface model which contains 12 Ce, 36 Hf and 96 O atoms, corresponding to 3 CeO_2 layers and 9 HfO_2 layers. The plane-wave cutoff is set to 550 eV. We use a $2 \times 2 \times 1$ Monkhorst-Pack k-point grid and an energy convergence threshold of 10^{-5} eV for structural optimizations. The bottom 6 HfO_2 layers (half of the HfO_2 layers) were fixed to their positions in the defect-free state during structural optimizations and NEB calculations, while the other layers were allowed to relax. We introduce oxygen vacancies at different positions in regions that allow relaxation to determine the migration energy barrier of oxygen vacancies. The minimum energy paths of oxygen vacancy diffusions are determined using the nudged elastic band (NEB) technique with VASP transition state tools[60]. The spring constant was set to 5 eV/Å^2, and a force convergence criterion of 0.03 eV/Å was used. The minimum energy paths of polarization switching in the CeO_2-HfO_2 system and pure polar HfO_2 are determined using the NEB technique implemented in the USPEX code[61–63] with lattice constants clamped during polarization switching. The root-mean-square forces on images smaller than 0.03 eV/Å is the halting criteria condition for NEB calculations. The variable elastic constant scheme is used, and the spring constant between the neighboring images is set in the range of 3.0–6.0 eV/Å^2.

Reporting summary

Further information on research design is available in the Nature Portfolio Reporting Summary linked to this article.

Data availability

The source data for Figs. 1–4 in this study are provided in the Source Data file. Source data are provided with this paper.

References

1. Scott, J. F. & Paz de Araujo, C. A. Ferroelectric memories. *Science* **246**, 1400–1405 (1989).
2. Zhou, C. et al. Enhanced polarization switching characteristics of HfO_2 ultrathin films Via acceptor-donor Co-doping. *Nat. Commun.* **15**, 2893 (2024).
3. Schroeder, U., Park, M. H., Mikolajick, T. & Hwang, C. S. The fundamentals and applications of ferroelectric HfO_2. *Nat. Rev. Mater.* **7**, 653–669 (2022).
4. Park, H. W., Roh, J., Lee, Y. B. & Hwang, C. S. Modeling of negative capacitance in ferroelectric thin films. *Adv. Mater.* **31**, 1805266 (2019).
5. Hao, Y. et al. Tuning negative capacitance in $PbZr_{0.2}Ti_{0.8}O_3/SrTiO_3$ heterostructures via layer thickness ratio. *Phys. Rev. Appl.* **16**, 034004 (2021).
6. Fina, I. & Sánchez, F. Epitaxial ferroelectric HfO_2 films: growth, properties, and devices. *ACS Appl. Electron. Mater.* **3**, 1530–1549 (2021).
7. Hoffmann, M., Slesazeck, S., Schroeder, U. & Mikolajick, T. What's next for negative capacitance electronics?. *Nat. Electron* **3**, 504–506 (2020).
8. Íñiguez, J., Zubko, P., Luk'yanchuk, I. & Cano, A. Ferroelectric negative capacitance. *Nat. Rev. Mater.* **4**, 243–256 (2019).
9. Cheema, S. S. et al. Ultrathin ferroic HfO_2–ZrO_2 superlattice gate stack for advanced transistors. *Nature* **604**, 65–71 (2022).
10. Mikolajick, T., Park, M. H., Begon-Lours, L. & Slesazeck, S. From ferroelectric material optimization to neuromorphic devices. *Adv. Mater.* **35**, 2206042 (2023).
11. Böscke, T. S., Müller, J., Bräuhaus, D., Schröder, U. & Böttger, U. Ferroelectricity in hafnium oxide thin films. *Appl. Phys. Lett.* **99**, 102903 (2011).
12. Cheema, S. S. et al. Enhanced ferroelectricity in ultrathin films grown directly on silicon. *Nature* **580**, 478–482 (2020).
13. Lee, H.-J. et al. Scale-free ferroelectricity induced by flat phonon bands in HfO_2. *Science* **369**, 1343–1347 (2020).
14. Park, S. H., Kim, J. Y., Song, J. Y. & Jang, H. W. Overcoming size effects in ferroelectric thin films. *Adv. Phys. Res.* **2**, 2200096 (2023).
15. Wei, Y. et al. A rhombohedral ferroelectric phase in epitaxially strained $Hf_{0.5}Zr_{0.5}O_2$ thin films. *Nat. Mater.* **17**, 1095–1100 (2018).
16. Ramaswamy, N. et al. NVDRAM: a 32Gb dual Layer 3D stacked non-volatile ferroelectric memory with near-DRAM performance for demanding AI workloads. In *Proc. International Electron Devices Meeting (IEDM)* 1–4 (IEEE, 2023).
17. Park, J. Y. et al. Revival of ferroelectric memories based on emerging fluorite-structured ferroelectrics. *Adv. Mater.* **35**, 2204904 (2023).
18. Salahuddin, S., Ni, K. & Datta, S. The era of hyper-scaling in electronics. *Nat. Electron* **1**, 442–450 (2018).
19. Zeng, B. et al. Polarization fatigue mechanism of laminated hafnium zirconium oxide ferroelectric thin films. *Acta Mater.***272**, 119920 (2024).
20. Yu, Y. et al. Intrinsic ferroelectricity in Y-doped HfO_2 thin films. *Nat. Mater.* **21**, 903–909 (2022).
21. Park, M. H., Kwon, D., Schroeder, U. & Mikolajick, T. Binary ferroelectric oxides for future computing paradigms. *MRS Bull.* **46**, 1071–1079 (2021).
22. Song, T. et al. Improved polarization and endurance in ferroelectric $Hf_{0.5}Zr_{0.5}O_2$ films on $SrTiO_3$ (110). *Nanoscale* **6**, 2337–2343 (2022).
23. de Araujo, C. A.-P., Cuchiaro, J. D., McMillan, L. D., Scott, M. C. & Scott, J. F. Fatigue-free ferroelectric capacitors with platinum electrodes. *Nature* **374**, 627–629 (1995).
24. Park, B. H. et al. Lanthanum-substituted bismuth titanate for use in non-volatile memories. *Nature* **401**, 682–684 (1999).
25. Shannigrahi, S. R. & Jang, H. M. Fatigue-free lead zirconate titanate-based capacitors for nonvolatile memories. *Appl. Phys. Lett.* **79**, 1051–1053 (2001).
26. Ramesh, R. et al. Ferroelectric La-Sr-Co-O/Pb-Zr-Ti-O/La-Sr-Co-O heterostructures on silicon via template growth. *Appl. Phys. Lett.* **63**, 3592–3594 (1993).
27. Jones, R. E. et al. Ferroelectric non-volatile memories for low-voltage, low-power applications. *Thin Solid Films.* **270**, 584–588 (1995).
28. Pešić, M. et al. Physical mechanisms behind the field-cycling behavior of HfO_2-based ferroelectric capacitors. *Adv. Funct. Mater.* **26**, 4601–4612 (2016).
29. Tagantsev, A. K., Stolichnov, I., Colla, E. L. & Setter, N. Polarization fatigue in ferroelectric films: basic experimental findings, phenomenological scenarios, and microscopic features. *J. Appl. Phys.* **90**, 1387–1402 (2001).
30. Shi, S. et al. Interface-engineered ferroelectricity of epitaxial $Hf_{0.5}Zr_{0.5}O_2$ thin films. *Nat. Commun.* **14**, 1780 (2023).
31. Nukala, P. et al. Reversible oxygen migration and phase transitions in hafnia-based ferroelectric devices. *Science* **372**, 630–635 (2021).
32. Noheda, B. Lessons from hafnium dioxide-based ferroelectrics. *Nat. Mater.* **22**, 562–569 (2023).
33. Lee, Y. B. et al. Oxygen-scavenging effects of added Ti layer in the TiN gate of metal-ferroelectric-insulator-semiconductor capacitor with Al-doped HfO_2 ferroelectric film. *Adv. Elect. Mater.* **8**, 2200310 (2022).
34. Kim, S. H. et al. Interfacial engineering of a $Mo/Hf_{0.3}Zr_{0.7}O_2/Si$ capacitor using the direct scavenging effect of a thin Ti layer. *Chem. Commun.* **57**, 12452–12455 (2021).
35. Alcala, R. et al. The electrode-ferroelectric interface as the primary constraint on endurance and retention in HZO-based ferroelectric capacitors. *Adv. Funct. Mater.* **33**, 2303261 (2023).
36. Tian, G. et al. Improved ferroelectricity and endurance of $Hf_{0.5}Zr_{0.5}O_2$ thin films in low thermal budget with novel bottom electrode doping technology. *Adv. Mater. Inter* **9**, 2102351 (2022).
37. Liu, Z. et al. Reversible fatigue-rejuvenation procedure and its mechanism in $Hf_{0.5}Zr_{0.5}O_2$ epitaxial films. *J. Phys. Condens. Matter* **35**, 204002 (2023).
38. Jiang, A. Q., Lin, Y. Y. & Tang, T. A. Charge injection and polarization fatigue in ferroelectric thin films. *J. Appl. Phys.* **102**, 074109 (2007).
39. Yang, T. J., Gopalan, V., Swart, P. J. & Mohideen, U. Direct observation of pinning and bowing of a single ferroelectric domain wall. *Phys. Rev. Lett.* **82**, 4106–4109 (1999).
40. Fengler, F. P. G. et al. Domain pinning: comparison of hafnia and PZT based ferroelectrics. *Adv. Electron. Mater.* **3**, 1600505 (2017).
41. Zhu, L. et al. Visualizing anisotropic oxygen diffusion in ceria under activated conditions. *Phys. Rev. Lett.* **124**, 056002 (2020).
42. Park, D.-S. et al. Induced giant piezoelectricity in centrosymmetric oxides. *Science* **375**, 653–657 (2022).
43. Yamamura, H., Takeda, S. & Kakinuma, K. Relationship between oxide-ion conductivity and dielectric relaxation in Sm-doped CeO_2. *Solid State Ion.* **178**, 889–893 (2007).
44. Zhang, Z. et al. Phase transformation driven by oxygen vacancy redistribution as the mechanism of ferroelectric $Hf_{0.5}Zr_{0.5}O_2$ fatigue. *Adv. Electron. Mater.* **10**, 2300877 (2024).

45. Yoo, I. K. & Desu, S. B. Mechanism of fatigue in ferroelectric thin films. *Phys. Status Solidi (A)* **133**, 565–573 (1992).
46. Kato, M., Watanabe, M., Hirooka, S. & Vauchy, R. Oxygen diffusion in the fluorite-type oxides CeO_2, ThO_2, UO_2, PuO_2, and $(U, Pu)O_2$. *Front. Nucl. Eng.* **1**, 1081473 (2023).
47. Nikolaenko, Y. M. et al. Non-uniform oxygen diffusion in epitaxial $La_{0.7}Sr_{0.3}MnO_{3-\delta}$ film on $SrTiO_3$ substrate. *J. Phys. D Appl. Phys.* **49**, 375302 (2016).
48. Li, J. et al. High endurance (>10^{12}) via optimized polarization switching ratio for $Hf_{0.5}Zr_{0.5}O_2$-based FeRAM. *Appl. Phys. Lett.* **122**, 082901 (2023).
49. Li, L. et al. Atomic-scale mechanisms of defect-induced retention failure in ferroelectrics. *Nano Lett.* **17**, 3556–3562 (2017).
50. Mueller, S., Muller, J., Schroeder, U. & Mikolajick, T. Reliability characteristics of ferroelectric Si:HfO_2 thin films for memory applications. *IEEE Trans. Device Mater. Reliab.* **13**, 93–97 (2013).
51. Zhang, Z., Wang, C., Yang, Y., Miao, X. & Wang, X. Polarization enhancement in $Hf_{0.5}Zr_{0.5}O_2$ capacitors induced by oxygen vacancies at elevated temperatures. *Appl. Phys. Lett.* **122**, 152902 (2023).
52. Xiong, K. et al. Epitaxial $Hf_{0.5}Zr_{0.5}O_2$ films: a temperature dependence study. *Appl. Phys. Lett.* **124**, 052901 (2024).
53. Prescher, C. & Prakapenka, V. B. *DIOPTAS*: a program for reduction of two-dimensional X-Ray diffraction data and data exploration. *High. Press. Res.* **35**, 223–230 (2015).
54. Perdew, J. P., Burke, K. & Ernzerhof, M. Generalized gradient approximation made simple. *Phys. Rev. Lett.* **77**, 3865–3868 (1996).
55. Kresse, G. & Furthmüller, J. Efficiency of ab-initio total energy calculations for metals and semiconductors using a plane-wave basis set. *Comput. Mater. Sci.* **6**, 15–50 (1996).
56. Kresse, G. & Furthmüller, J. Efficient iterative schemes for ab initio total-energy calculations using a plane-wave basis set. *Phys. Rev. B* **54**, 11169–11186 (1996).
57. Da Silva, J. L. F., Ganduglia-Pirovano, M. V., Sauer, J., Bayer, V. & Kresse, G. Hybrid functionals applied to rare-earth oxides: the example of ceria. *Phys. Rev. B* **75**, 045121 (2007).
58. Nolan, M. Enhanced oxygen vacancy formation in ceria (111) and (110) surfaces doped with divalent cations. *J. Mater. Chem.* **21**, 9160–9168 (2011).
59. Nolan, M., Parker, S. C. & Watson, G. W. The electronic structure of oxygen vacancy defects at the low index surfaces of ceria. *Surf. Sci.* **595**, 223–232 (2005).
60. Henkelman, G., Uberuaga, B. P. & Jónsson, H. A climbing image nudged elastic band method for finding saddle points and minimum energy paths. *J. Chem. Phys.* **113**, 9901–9904 (2000).
61. Oganov, A. R., Lyakhov, A. O. & Valle, M. How evolutionary crystal structure prediction works—and why. *Acc. Chem. Res.* **44**, 227–237 (2011).
62. Lyakhov, A. O., Oganov, A. R., Stokes, H. T. & Zhu, Q. New developments in evolutionary structure prediction algorithm USPEX. *Comput. Phys. Commun.* **184**, 1172–1182 (2013).
63. Oganov, A. R. & Glass, C. W. Crystal structure prediction using ab initio evolutionary techniques: principles and applications. *J. Chem. Phys.* **124**, 244704 (2006).

Acknowledgements

This work was supported by National Key R&D Program of China (Grant No. 2021YFA1202100), the National Natural Science Foundation of China (Grant Nos. 92477129, 52372105, 12361141821, and U24A2013), the Guangdong Basic and Applied Basic Research Foundation (Grant No. 2024B1515120010), and Shenzhen Science and Technology Program (Grant No. KQTD20200820113045083). Z.H.C. has been supported by the State Key Laboratory of Precision Welding & Joining of Materials and Structures (Grant No. 24-Z-13) and "the Fundamental Research Funds for the Central Universities" (Grant No. 2024FRFK03012). S.D. acknowledges Science and Engineering Research Board (EEQ/2023/000089), Infosys Young Investigator award and Indian Institute of Science start up grant for financial support. The computational resource was provided by Westlake HPC Center. The authors thank the staff from Shanghai Synchrotron Radiation Facility (SSRF) at BL15U1.

Author contributions

Z.H.C. and C.Z. conceived and designed the research. Z.H.C. supervised this study. C.Z. fabricated the films and carried out electric measurements with the assistance of Y.Y.S., H.L.W. and J.X.L. C.Z. performed the XRD measurements with the assistance of H.L.H., S.Z.H., C.Y.K. and Y.Y.S. Y.P.F. and Y.L.T. performed the STEM characterizations. L.Y.M. and S.L. carried out theoretical calculations. C.Z., L.Y.M., S.L., S.D. and Z.H.C. wrote the manuscript. All authors discussed the results and commented on the manuscript.

Competing interests

The authors declare no competing interests.

Additional information

Supplementary information The online version contains supplementary material available at https://doi.org/10.1038/s41467-025-63048-3.

Correspondence and requests for materials should be addressed to Yunlong Tang, Shi Liu or Zuhuang Chen.

Peer review information *Nature Communications* thanks Atul Thakre and the other, anonymous, reviewer(s) for their contribution to the peer review of this work. A peer review file is available.